J. Electrochem. Sci. Eng. **16** (2026) 3234; https://doi.org/10.5599/jese.3234

Open Access : : ISSN 1847-9286
https://pub.iapchem.org/ojs/index.php/JESE

Original scientific paper

Comparative study of 2D perovskite cathodes: impact of organic cation variation on electrochemical performance in lithium-ion batteries

Alfredo Romero-Contreras, Nora Aleyda García Gómez and Eduardo Sánchez-Cervantes✉

Facultad de Ciencias Químicas, Universidad Autónoma de Nuevo León, Mexico

Corresponding Author: ✉eduardo.sanchezcv@uanl.edu.mx

Received: January 16, 2026; Accepted: April 14, 2026; Published: April 17, 2026

Abstract

In this study, two organic-inorganic hybrid perovskites, butylammonium copper chloride (BACC) and methylammonium copper chloride (MACC), were synthesized and evaluated as feasible active cathode materials for lithium-ion batteries. Both compounds were structurally and morphologically characterized using X-ray diffraction, scanning electron microscopy and infrared spectroscopy, revealing high crystalline structures and well-defined morphologies consistent with long-range order and unique features of conversion materials. The electrochemical performance of synthesized compounds as cathodes was assessed through cyclic voltammetry and galvanostatic charge/discharge measurements. Butylammonium copper chloride, with formula $(C_4H_{12}N)_2CuCl_4$, exhibited a remarkable specific discharge capacity of 200 mAh g^{-1} at 20 mA g^{-1} with capacity retention close to 65 %. Meanwhile, methylammonium copper chloride $(CH_3NH_3)_2CuCl_4$ delivered a specific capacity of 160 mAh g^{-1} at 20 mA g^{-1}, maintaining 90.2 % capacity retention. Post-cycling XRD analysis was carried out on the cathodes after 100 cycles of operation at 50 mA g^{-1}, providing evidence of structural changes during battery operation. These structural transformations account for the gradual capacity fading observed during prolonged cycling and demonstrate that a Coulombic efficiency close to 100 % does not necessarily imply structural reversibility. Overall, the results indicate that BACC and MACC should be regarded as model systems for fundamental studies of copper electrochemical chemistry in halogenated hybrid perovskites, rather than as competitive cathode materials for practical lithium-ion battery applications.

Keywords

Li-ion battery cathode; copper-based materials; halogenated hybrid perovskites; cyclic stability; battery postmortem XRD

Introduction

As the demand for efficient, high-capacity, and sustainable batteries increases, novel materials that can enhance their performance and stability are required. Approaches to improving the battery's performance, such as modifying the stoichiometry or introducing dopants, have shown limited potential and only modest improvements in stability and capacity [1-3]. To overcome these challenges, hybrid perovskite structures have gained attention, emerging as new candidates as active cathode compounds due to their flexibility, electric conductivity and stability. These materials have been investigated in diverse areas of interest such as photovoltaic applications [4], piezoelectric generators [5], photonics technologies [6] and energy storage devices [7].

Early developments in hybrid materials for energy storage applications were presented by Vicente *et al*. [8], who applied for the first time the $CH_3NH_3PbBr_3$ and $CH_3NH_3PbI_3$ hybrid perovskites as anode materials in lithium-ion batteries. The first discharge capacity for $CH_3NH_3PbBr_3$ was 331.8 mAh g^{-1} at a current density of 200 mA g^{-1}. This value is comparable to that of commercially available graphite. After 30 cycles, the capacity decreased to 157.4 mA h g^{-1} with a retention efficiency of 76.9 % [8].

However, since lead-based compounds were found to be dangerous for the environment, their use has been restricted and the intention to replace them with environmentally friendly compounds has increased the activity in synthesizing perovskites based on transition metals (*e.g*. Sn, Pb, Ge) halides [9-11]. Unfortunately, their practical application is limited by poor solubility and moisture instability. In contrast, copper halide perovskites possess good solubility and stability.

Cu-based materials possess exceptional features which include tailorable band edges, excellent intrinsic hole-transporting effects and good electronic conductivity. To optimize their characteristics for potential energy storage applications, some authors have explored the structural effects of hybrid copper chloride perovskites by incorporating a wide variety of organic cations to form two-dimensional structures [12].

Recently, several compounds have been synthesized by adding dimethylammonium (DMA^+) and acetamidinium (Ac^+) as organic cations in the CuCl system, proving the formation of five new crystalline phases: $DMACu_2Cl_3$, $DMACuCl_2$, $DMA_4[Cu_2Cl_6]$, DMA_3CuCl_4, and $AcCuCl_2$, demonstrating the flexibility of chlorocuprates to be linked to new organic cations [13]. Additional efforts have evaluated and optimized the synthesis of more complex structures, such as bis(dodecylammonium) tetrachlorocuprate $(C_{12}H_{28}N)_2CuCl_4$, for thermal energy storage, highlighting the potential of chlorocuprates as phase-change materials for energy storage via polymorphic transitions [14].

In addition, a small group of reports emphasizes the incorporation of novel organic counterparts in chlorocuprates, such as benzylamine. Previous research has shown that the material studied in this work, $(C_6H_5CH_2NH_3)_2[CuCl_4]$ (BZACC: benzylamine copper chloride) is known to have a 2D layered perovskite structure with successive magnetic phase transitions which provide BZACC with strong ferromagnetic properties [15]. Also, BZACC has been used as a precursor for oxidation reactions to obtain new Cu-based materials [16] and to better understand the role of CuCl as well as $CuCl_2$ in organic synthesis [17].

Although all the research has been based on copper as the metallic cation, the electrochemical properties of those copper-based materials have not yet been identified or measured, nor has their performance as a chemical energy material in storage devices. The incorporation of butylammonium, a long-chain organic ammonium cation, has been reported only for its application in solar cells and the introduction of methylammonium is limited to its application in Pb-based materials [18].

Organic copper chlorides are promising active components for lithium battery systems due to their combination of inorganic and organic properties. The high conductivity related to copper presence,

the laminar structure of perovskites and easy synthesis make them potential candidates for improving battery efficiency, longevity, and performance, thus contributing to the advancement of next-generation lithium-ion batteries. This work is focused on the synthesis, characterization and application of two 2D hybrid perovskites, butylammonium copper chloride (BACC) and methylammonium copper chloride (MACC), as active materials for cathode applications for lithium-ion batteries.

Experimental

Synthesis of butylammonium copper chloride

First, butylammonium chloride ($C_4H_9NH_3Cl$) was synthesized *via* an acid-base reaction between butylamine (Sigma-Aldrich, 98 %) and hydrochloric acid (Sigma-Aldrich, 37 wt.% in H_2O) in a 1:1 molar ratio. The reaction was performed in an ice bath to control its exothermic nature and prevent overheating. For the synthesis of BACC, the compound was prepared at room temperature by mixing a stoichiometric amount of $CuCl_2{\cdot}2H_2O$ (Sigma-Aldrich, 98 %) with butylammonium chloride in ethanol. Single crystals of the product were obtained through slow evaporation of the solution at 70 °C. Upon addition of the butylammonium chloride to the copper (II) chloride solution, the mixture turned green, and after solvent evaporation, a yellow precipitate was formed. The resulting crystals were collected and dried at 70 °C in a vacuum furnace.

Synthesis of methylammonium copper chloride

MACC single crystals were prepared by mixing $(CH_3NH_4)Cl$ and $CuCl_2{\cdot}2H_2O$ in distilled water under stirring at a molar ratio of 2:1. The solvent was then evaporated at 60 °C for 24 h, resulting in a golden powder. The synthesized crystals were harvested and dried under vacuum at 70 °C.

Battery fabrication

A mixture of BACC or MACC powder, carbon black (Super P, TIMCAL), and polytetrafluoroethylene (PTFE) powder (Sigma-Aldrich) was prepared in a 60:30:10 weight ratio. The components were manually blended until a homogeneous paste was obtained. This paste was then roll-pressed and uniformly applied onto a stainless-steel mesh current collector. The resulting cathodes were subsequently dried under vacuum at 60 °C for 24 hours to eliminate residual moisture. The average active material loading was about 4.2 mg cm^{-2}.

Coin-type cells were assembled in an argon-filled glove box. Pure lithium foil was used as the counter and reference electrode, and the prepared cathode served as the working electrode. To separate both electrodes, a microporous separator (Celgard 2325-1750-A) was inserted. For the electrolyte solution, commercial $LiPF_6$ electrolyte (Sigma Aldrich) was incorporated.

For characterization, the crystal structures of BACC and MACC were studied by X-ray diffraction (XRD) using a D2-Phaser (Bruker) with Cu Kα radiation (λ = 0.15418 nm) at a scanning rate of 0.05° s^{-1} over an angle range of 5 to 50°. Scanning Electron Microscope images were taken using a JSM-6701F instrument from JEOL. The infrared spectrum was recorded at room temperature within the 1000 to 3500 cm^{-1} spectral range with a 4 cm^{-1} resolution using an Interspec 200-X FT IR spectrometer.

Finally, the electrochemical characterization was performed using cyclic voltammetry, which was acquired with a MacPile II at a scan rate of 0.125 mV s^{-1} over a voltage range from 0.01 to 2 V *vs*. Li/Li^+. Charge/discharge tests were performed on a multichannel battery cycler BTS-3500 (Neware Electronic Co.) within the same voltage range at different current rates (from 20 to 500 mA g^{-1}).

Electrochemical impedance spectroscopy (EIS) measurements of the MACC and BACC materials were performed using a BioLogic VMP3 potentiostat/galvanostat in a battery coin configuration.

The impedance spectra were recorded in the frequency range from 100 kHz to 100 mHz, sweeping from high to low frequency, with 10 points per decade to ensure adequate frequency resolution. A sinusoidal current perturbation with an amplitude of 3 µA was applied to maintain linear response conditions. All measurements were conducted at room temperature under open-circuit potential after stabilization. EIS was performed both prior to cycling (initial state) and after 200 galvanostatic charge-discharge cycles.

Results and discussion

Structural properties of BACC and MACC were confirmed by X-ray diffraction measurements on the synthesized powders at room temperature; the X-ray patterns are shown in Figure 1. Figure 1a shows the XRD of BACC, the labelled peaks correspond to their typical crystallographic reflections located at 2θ = 5.8, 11.6, 17.4, 24, 29.1, 35, 41 and 47.3°, which correspond to the planes (00*k*) where *k* = 2, 4, 6, 8, 10, 12, 14, 16. All the signals match those reported in literature, confirming the high crystallinity of the BACC sample [19]. Its structural arrangement includes the anion $(CuCl_4)^{2-}$, which forms a corner-sharing octahedra in which each Cu^{2+} ion is coordinated by four Cl^- ions in a square-planar geometry. The organic layer is composed of butylammonium cations ($C_4H_9NH_3^+$), which generate the laminar disposition between the $(CuCl_4)^{2-}$ octahedra. Figure 1b displays the XRD pattern of MACC. The peaks are labelled according to their symmetrical plane corresponding to the reflections of (100), (001), (21-1), (020), (300), (310), (122) and (22-2), indicating the highly crystalline perovskite structure obtained. Based on our results, the crystallites belong to the orthorhombic system with space group Pbca, consistent with reports in the literature [20]. Regarding the structure of MACC, it consists of an inorganic layer composed of $CuCl_6$ octahedra and an organic layer of $C_6H_5CH_2NH_3$ which extends between the $CuCl_6$, the hydrogen of the ammonium cation bonds to the halogens of the inorganic layer, and the organic R-group extends into the space between the inorganic layers [21,22] in a strong preferential orientation, typical of a 2D perovskite structure. A diagram of the BACC and MACC structures is displayed in Insets C and D, respectively, inside Figure 1.

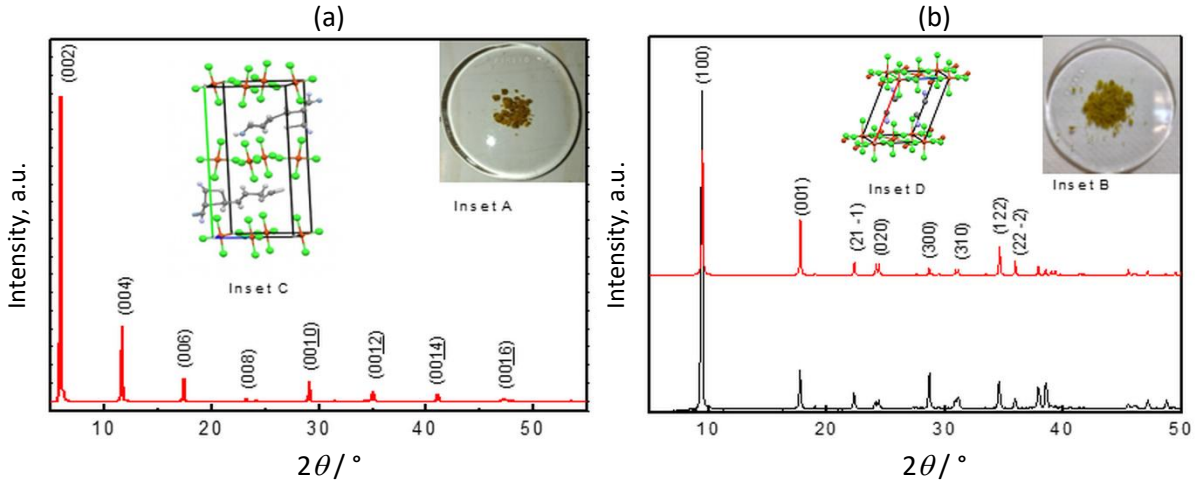

Figure 1. *X-ray diffraction patterns of a) butylammonium copper chloride (BACC) and b) methylammonium copper chloride (MACC). All the peaks match those reported in literature for both compounds. Inset A shows an image of BACC powder and Inset B depicts a MACC powder image after dried process. Insets C and D represent structural diagrams of BACC and MACC samples, respectively, where red, green, purple and white spheres represent copper, chlorine, carbon and hydrogen atoms, respectively*

Further experiments to elucidate the structural properties of both active materials were carried out using IR measurements, and the obtained spectra for BACC and MACC are shown in Figures 2a

and 2b, respectively. The functional groups were identified based on their vibrational assignments, which are summarized in Tables 1 and 2 for BACC and MACC, respectively. The FTIR analysis confirms the successful synthesis of the hybrid materials. The spectra of BACC and MACC exhibit the characteristic vibrational modes associated with protonated alkylammonium cations, including the N-H stretching and bending modes of NH_3^+, as well as the C-H stretching and deformation bands corresponding to the alkyl chains [23,24]. Additionally, the presence of N-C stretching modes, together with the C-H stretching and bending vibrations associated with CH_2 and CH_3 groups, confirms the successful incorporation of butylammonium and methylammonium species into the hybrid structure.

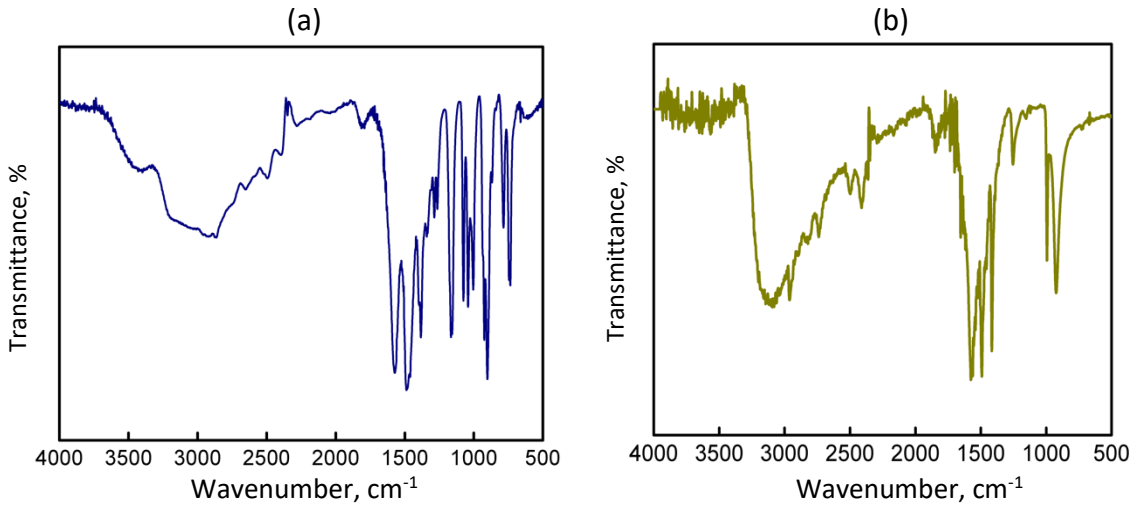

Figure 2. *IR spectra of a) BACC and b) MACC perovskite. bands corresponding to the vibrational modes of butylamine and methylamine are identified and indexed*

Table 1*. FTIR vibrational modes and band assignments of butylammonium copper chloride (BACC)*

Wavenumber, cm^{-1}	Vibrational assignment	Functional group
3300 to 3150	ν(N-H) asymmetric and symmetric stretching	NH_3^+ (butylammonium)
3000 to 2850	ν(C-H) asymmetric and symmetric stretching	$-CH_2/-CH_3$ (butyl chain)
~1570	δ(N-H) bending (scissoring)	NH_3^+
1509 to 1460	$\delta(CH_2)$ and $\delta(CH_3)$ bending	Aliphatic alkyl chain
1395 to 1380	$\delta(CH_3)$ symmetric bending	Alkyl group
1165 to 1040	ν(C-N) stretching	Protonated amine
925 to 900	NH_3^+ rocking mode	Butylammonium cation

Table 2*. FTIR vibrational modes and band assignments of methylammonium copper chloride (MACC)*

Wavenumber, cm^{-1}	Vibrational assignment	Functional group
3300-3100	ν(N-H) asymmetric and symmetric stretching	NH_3^+ (methylammonium)
3020-2950	ν(C-H) stretching	$-CH_3$
~1580-1560	δ(N-H) bending (scissoring)	NH_3^+
1470-1450	$\delta(CH_3)$ asymmetric bending	Methyl
1410-1390	$\delta(CH_3)$ symmetric bending	Methyl
1150-1050	ν(C-N) stretching	Protonated amine

The electrochemical performance of the BACC material was investigated using cyclic voltammetry (CV), galvanostatic charge-discharge (GCD), cycling stability, and rate capability measurements. These complementary techniques provide insight into the lithium storage mechanism, reversibility, and structural stability of the material during electrochemical cycling. The cyclic voltammetry profiles recorded between 0.01 and 2.0 V (Figure 3a) exhibit reproducible redox features across multiple cycles. During the first cathodic scan, a reduction peak cantered around

0.28 V is observed, which can be attributed to lithium insertion into the copper chloride framework and the formation of a solid electrolyte interphase (SEI). In the anodic scan, a broad oxidation peak near 1.12 V corresponds to lithium extraction and partial reversibility of the redox process involving the Cu-Cl network. The subsequent cycles show nearly overlapping CV curves, indicating good electrochemical reversibility after the initial activation process.

The galvanostatic charge-discharge profiles measured at different current densities (Figure 3b) reveal the lithium storage behaviour of BACC. At a low current density of 20 mA g^{-1}, the material delivers a high discharge capacity of around 200 mAh g^{-1}. When the current density is increased to 50 mA g^{-1}, the discharge capacity decreases to around 140 mAh g^{-1}, reflecting moderate kinetic limitations while still maintaining good reversibility. Further increasing the current density to 100 mA g^{-1} results in a discharge capacity of approximately 100 mAh g^{-1}, demonstrating that BACC can retain a significant fraction of its capacity under higher rate conditions. At higher current densities of 200 and 500 mA g^{-1}, the discharge capacities decrease to approximately 60 and 23 mAh g^{-1}, respectively. This gradual capacity fading with increasing current density is mainly associated with increased polarization effects and limited lithium-ion diffusion at fast charge-discharge rates [25].

As the current density increases, a gradual decrease in capacity is observed, which is typical of diffusion-limited processes; however, the overall shape of the charge-discharge curves is well preserved, indicating good kinetic properties. The sloping voltage plateaus observed during discharge and charge processes are consistent with a combined faradaic and pseudocapacitive lithium storage mechanism [26,27].

Furthermore, the cycling stability of BACC was evaluated over 100 cycles at a fixed current density (see Figure 3c). The material exhibits an initial discharge capacity of approximately 150 mAh g^{-1}, followed by a gradual and moderate capacity decay upon prolonged cycling. Notably, the coulombic efficiency remains nearly 100 % after the first few cycles and remains stable, demonstrating excellent reversibility of the lithium insertion/extraction processes in each cycle.

The rate capability performance plotted in Figure 3d reveals the ability of BACC to sustain lithium storage under varying current densities. As the current density increases from 20 to 500 mAg^{-1}, the capacity decreases progressively, reflecting increased polarization and kinetic limitations. Interestingly, when the current density is returned to 20 mA g^{-1}, a substantial recovery of capacity is observed, indicating good reversibility. This behaviour highlights the favourable charge-transport and ion-diffusion characteristics of BACC material.

On the other hand, MACC showed a distinctive behaviour which is described in the following paragraphs. Figure 4a shows the cyclic voltammetry (CV) profiles of the MACC electrode recorded over five consecutive cycles within the voltage window of 0.01-2.0 V *vs*. Li^+/Li. The CV curves exhibit highly overlapping shapes after the first cycle, indicating good electrochemical reversibility of the MACC material during repeated lithiation and delithiation processes. A broad cathodic feature cantered around 0.4 V can be associated with lithium insertion into the MACC structure and possible interfacial reactions, while the anodic peak near 1.0 V corresponds to the reversible lithium extraction process. Figure 4b presents the galvanostatic charge-discharge profiles of MACC measured at different current densities ranging from 20 to 500 mA g^{-1}. At a low current density of 20 mA g^{-1}, the electrode delivers a discharge capacity of 160 mAh g^{-1}, demonstrating efficient lithium storage capability.

As the current density increases to 50, 100, 200 and 500 mA g^{-1}, the discharge capacity gradually decreases to about 102, 67, 29 and 8 mAh g^{-1}, respectively. This trend is attributed to kinetic limitations and increased polarization at higher current densities, which restrict lithium-ion diffusion and charge transfer processes.

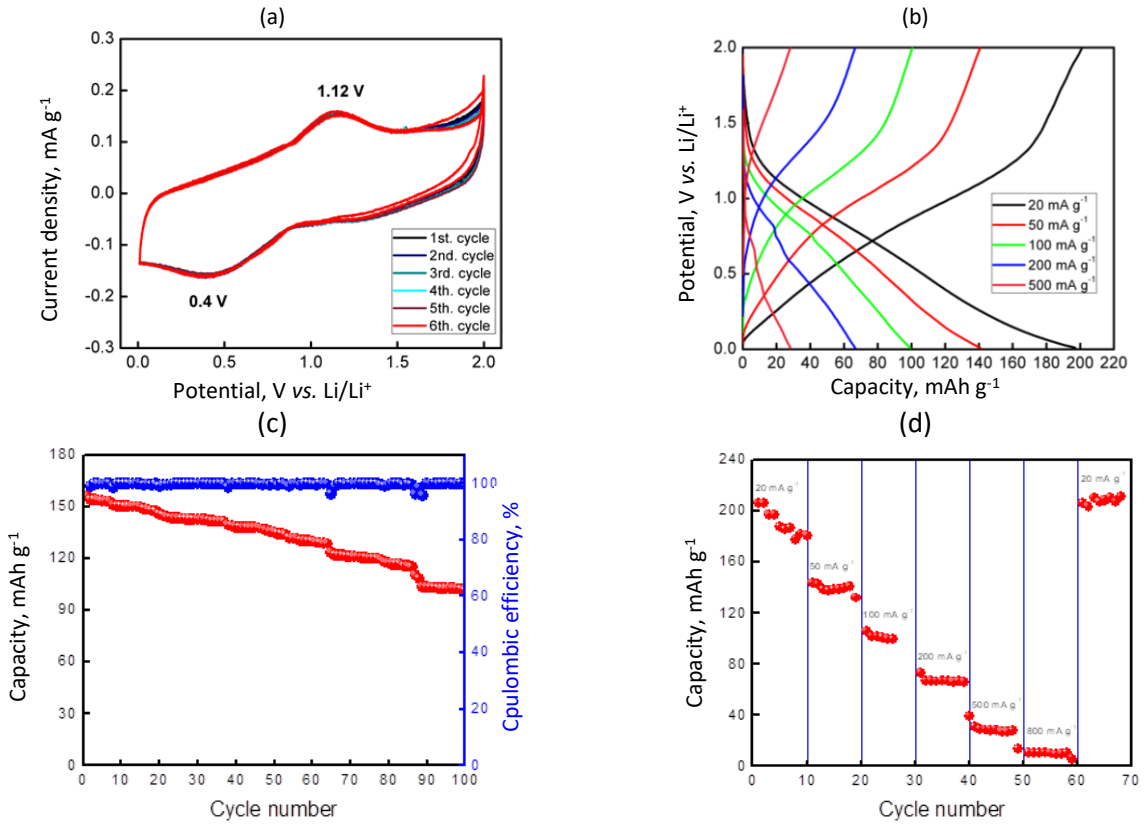

Figure 3. *Electrochemical characterization of BACC based batteries: a) cyclic voltammetry curves of the BACC perovskite recorded at a scan rate of 0.125 mV s^{-1}, b) charge-discharge voltage profiles of BACC measured at current rates ranging from 20 to 200 mA g^{-1}, c) cycling performance and capacity retention of BACC at 50 mA g^{-1}, d) rate capability of the BACC material under different current densities between 20 and 200 mA g^{-1}*

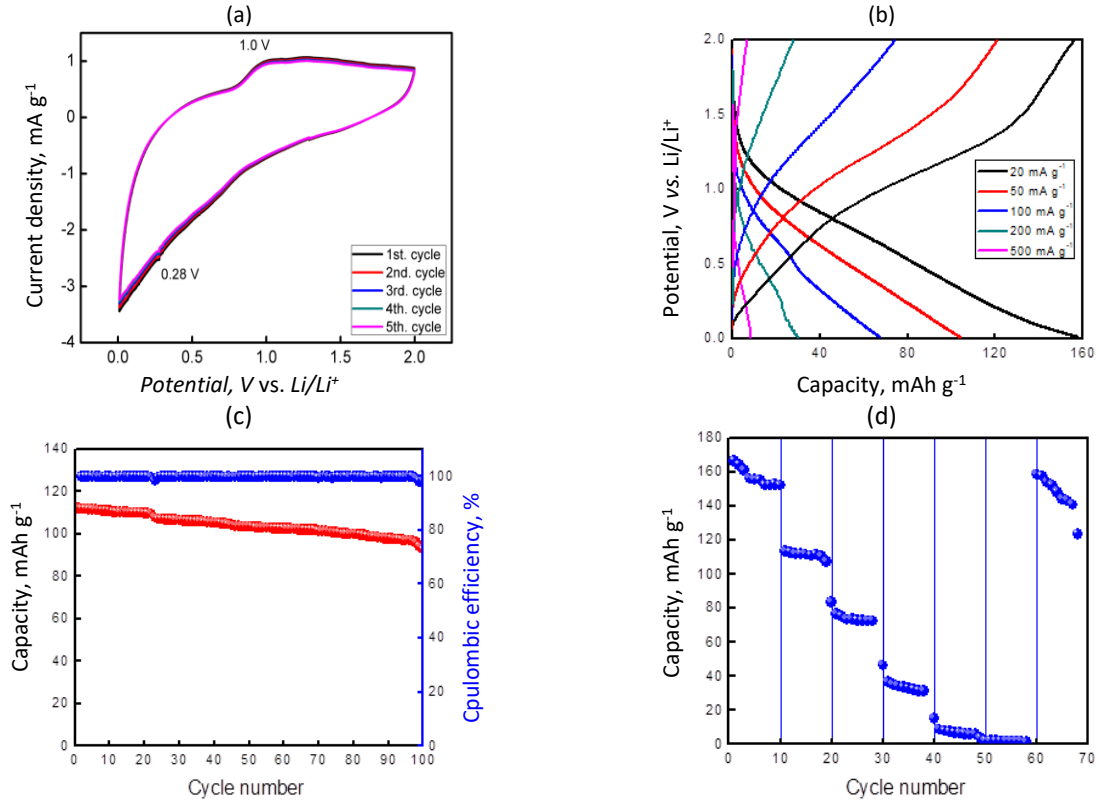

Figure 4. *Electrochemical performance of MACC-based batteries: a) cyclic voltammetry curves of MACC perovskite measured at 0.125 mV s^{-1} rate, b) charge and discharge profiles for MACC at several current rates from 20 to 200 mA g^{-1}, c) cycle stability and capacity retention of MACC at 50 mA g^{-1}, d) rate capability of MACC at various current densities ranging from 20 mA g^{-1} to 200 mA g^{-1}*

The cycling performance of MACC is shown in Figure 4c, where the electrode exhibits an initial capacity close to 113 mAh g^{-1} at 50 mA g^{-1}, followed by a gradual capacity decay to 93 mAh g^{-1} after 100 cycles. Despite this moderate capacity fading, the coulombic efficiency remains close to 100 % throughout the cycling test. This behaviour should not be interpreted as evidence of full structural reversibility, as confirmed by the post-mortem XRD analysis. Moreover, Figure 4d illustrates the rate capability of the MACC electrode as current density increases. The capacity decreases systematically from 160 mAh g^{-1} at 20 mA g^{-1} to 110, 75, 35, and 5 mAh g^{-1} at 50, 100, 200 and 500 mA g^{-1}, respectively. Notably, when the current density is returned to 20 mA g^{-1}, the electrode partially recovers its capacity (between 140 and 150 mAh g^{-1}).

A comparison regarding the electrochemical performance of both materials reveals notable differences in lithium storage behaviour, which can be attributed to the distinct alkylammonium cations present in their structures. While both materials exhibit stable CV profiles and high coulombic efficiency, BACC generally delivers higher reversible capacities and superior rate performance compared to MACC. This enhancement is likely related to the longer butyl chain in BACC, which may promote increased interlayer spacing and facilitate lithium-ion diffusion. In contrast, MACC shows slightly lower capacities and more pronounced capacity decay at high current densities, suggesting more limited ion transport pathways. Nevertheless, both compounds demonstrate good electrochemical reversibility, confirming their potential as organic-inorganic hybrid electrode materials for lithium-ion storage applications. The observed decrease in capacity over time in Figures 3d and 4d might be related to changes in the structural properties of both compounds.

To further investigate this point, electrochemical impedance spectroscopy was performed over batteries prior to cycling and after 200 cycles. In particular, EIS is a powerful tool for assessing the impact of cycling on the internal resistance and overall stability of cathode materials, enabling a more comprehensive understanding of their performance and degradation mechanisms. The corresponding BACC and MACC spectra are depicted in Figures 5a and 5b, respectively.

For both samples, the impedance spectra show that the high-frequency interception on the real axis (Z') remains low and essentially unchanged after cycling. This feature is commonly associated with electrolyte resistance, and its stability indicates that the bulk electrolyte contribution is not significantly affected, suggesting that the observed changes predominantly originate from processes occurring within the electrode. Regarding semicircle behaviour, clear differences are observed between the two materials upon cycling. For the BACC-based cathode, a small semicircle is observed before cycling, indicating low total resistance, as suggested by the low-frequency intercept on the real axis. This feature reflects a limited overall system impedance at this early stage, suggesting minimal transport limitations and an intact active material structure. However, after 200 cycles, the semicircle extends and presents a much larger impedance response, with a significant shift of the low-frequency intercept toward larger Z'. This change indicates a strong increase in total resistance, which can be associated with restricted ion transport, loss of conductive pathways, and the development of resistive interphases within the electrode, evidencing substantial degradation of the active material.

Overall, the comparison between the two materials highlights a clear difference in their response to cycling. While BACC undergoes a more pronounced evolution characterized by a strong distortion and loss of definition of the semicircle related to its transport-limited behaviour, MACC retains a discernible semicircle after cycling, indicating that the charge-transfer process remains operative and that an electrochemical response is still preserved, despite a significant increase in resistance. These observations indicate that the BACC system shows a more severe loss of electrochemical functionality, whereas MACC preserves a partially operative charge-transfer process even after prolonged cycling.

According to the capacity measurements presented in Figures 3c and 4c, BACC shows a rapid loss of capacity, which is consistent with the severe increase in impedance and the suppression of the charge-transfer process, whereas the slower decay observed for MACC correlates with the preservation of a partially and larger operative electrochemical response. Together, these results suggest that although both materials degrade, BACC undergoes a more drastic loss of electrochemical functionality, while MACC maintains a comparatively more stable behaviour during cycling.

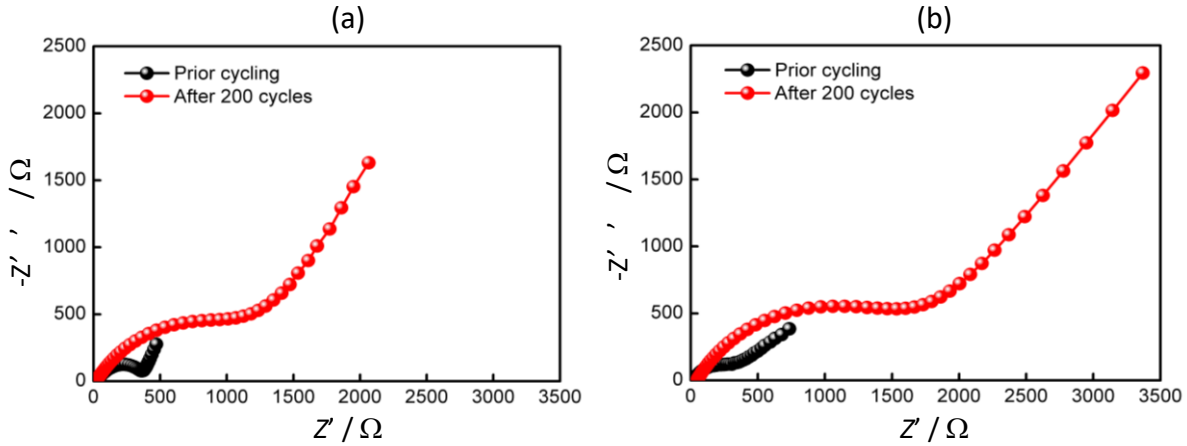

Figure 5. *Electrochemical impedance spectra of (a) BACC and (b) MACC batteries measured prior to cycling and after 200 charge/discharge cycles*

The EIS analysis thus provides clear evidence that the long-term stability of the BACC and MACC materials is compromised by active-material degradation. Such degradation is expected to directly impact the kinetics of charge storage, particularly by limiting lithium-ion diffusion and promoting surface-controlled processes [28,29].

Earlier works have explored the electrochemical response of Cu-based compounds, which decompose into several byproducts after several charge-discharge cycles. Poizot *et al.* [30] demonstrated that the electrochemical reduction of CuO proceeds through a conversion reaction forming metallic Cu and Li_2O, which is associated with partial irreversibility and structural reconstruction. Subsequent investigations on CuO have shown that repeated cycling leads to particle pulverization, loss of electrical contact, and accumulation of electrochemically inactive phases, ultimately resulting in capacity fading and reduced Coulombic efficiency [31].

Similarly, copper halides, such as $CuCl_2$, have been reported to undergo conversion reactions accompanied by halide redistribution and dissolution effects, which contribute to structural instability during cycling. Studies on copper halide electrodes indicate that these materials often exhibit high initial capacities and apparent pseudocapacitive features, which progressively evolve due to surface reconstruction and partially irreversible redox processes involving $Cu^{2+}/Cu^{+}/Cu^{0}$ transitions [32].

In addition, hybrid copper-based materials, including organic-inorganic copper halide frameworks, have shown capacitive electrochemical responses arising from fast surface redox reactions [33]. Nevertheless, several reports emphasize that such pseudocapacitive behaviour may originate from metastable surface states and reconstruction phenomena, rather than from stable charge storage. As highlighted by Brousse *et al.* [34], elevated capacitive contributions in transition metal-based systems may mask underlying degradation mechanisms linked to conversion reactions.

To clarify whether the reported electrochemical response arises from an intercalation or conversion mechanism, XRD measurements were performed over the composite cathodes in their pristine state and after the first charge-discharge cycle. The electrodes were analysed directly to determine whether the main crystalline phase remained present after cycling.

Figure 6a presents the XRD patterns of the pristine BACC cathode in comparison with those obtained after the first discharge-charge cycle. As observed, the characteristic diffraction peaks of crystalline BACC are clearly preserved in the pristine electrode, confirming that the main phase remains structurally without changes within the composite. In addition, a broad diffraction feature observed between 20° and 30° is attributed to the amorphous contribution of super P carbon, which generates the diffuse background. Similar broad diffraction features have been widely reported in composite battery electrodes containing conductive carbon additives. In several studies, including Si/C and transition metal-based composite systems, a diffuse halo typically observed 2θ between 20 and 30° has been attributed to the amorphous structure of carbon materials such as Super P [35].

In the case of MACC material, the XRD patterns prior and after cycling are presented in Figure 6b. Clearly, the main peaks associated with low diffraction angles disappear after cycling and their intensity is also affected by the incorporation of carbon during composite formation. Some reflections at higher diffraction angles are still detectable in the diffractogram; however, their intensity is partially masked by the diffraction signals arising from the stainless-steel mesh (the main peaks associated with its presence it is located at 29°) and the presence of carbon.

The strong attenuation of the principal X-ray diffraction reflections of both active materials after the first charge-discharge cycle is an important indicator of the underlying electrochemical storage mechanism. In intercalation-type electrodes, lithium insertion-extraction occurs, preserving the long-range order with only small peak shifts or slight broadening in ex-situ XRD patterns. In contrast, materials undergoing conversion reactions typically exhibit a substantial loss of crystallinity after initial cycles, as the initial structure is transformed into new phases.

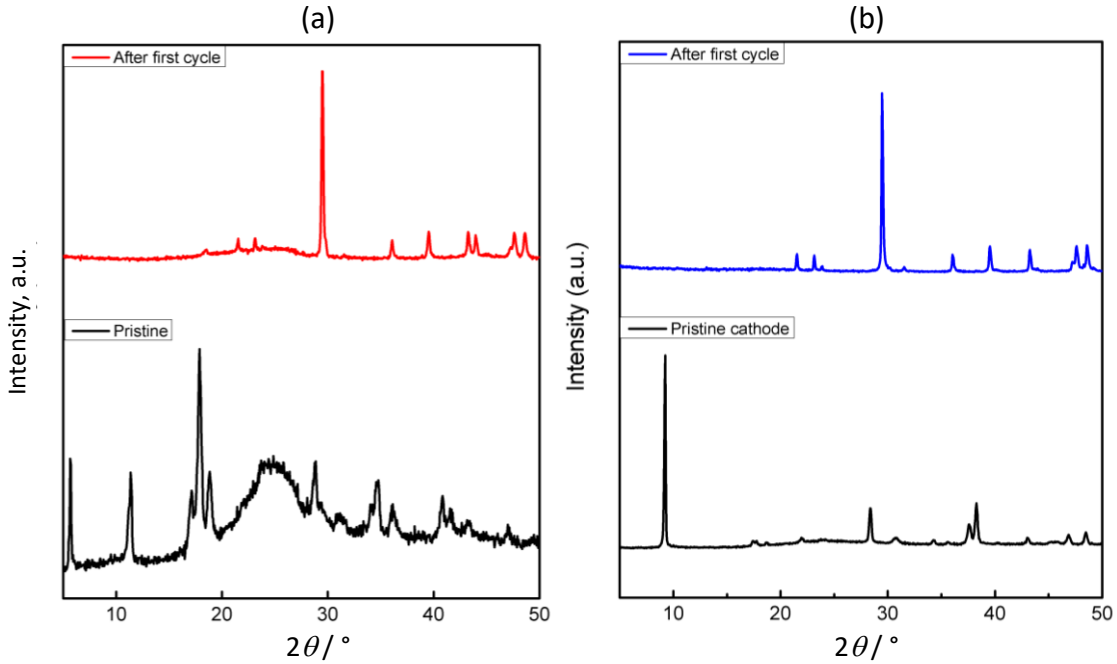

Figure 6. *X-ray diffraction patterns of composite cathodes: (a) BACC and (b) MACC, measured in their pristine form and after the first charge-discharge cycle*

More recent work on transition-metal oxide systems has corroborated that the disappearance of principal peaks after early cycles can be attributed to the breakdown of long-range order and formation of nano-scaled products [30]. For example, Lin *et al*. reported similar phase evolution in conversion-type electrodes, where XRD reflections of the original compound progressively weaken and are replaced by diffuse scattering as cycling progresses [36]. Wang *et al*. further confirmed that conversion reactions for binary metal fluorides lead to significant attenuation of the initial phase

reflections, forming product phases that are often poorly crystalline [37]. Additionally, operando XRD studies have further clarified the structural evolution occurring during the initial lithiation process. Belmonte et al. demonstrated that, during the first discharge of a perovskite-based electrode, the diffraction peaks of the pristine phase progressively decrease in intensity and eventually vanish as the reaction proceeds through a conversion stage. This evolution reflects the breakdown of the original long-range order and the formation of new phases rather than simple lithium insertion within a preserved host lattice. Such behaviour highlights that the disappearance of principal reflections during early cycling can be intrinsically linked to a conversion-type storage mechanism [38].

To further elucidate the structural changes suggested from the electrochemical performance of both compounds, post-mortem XRD analyses were performed on cathodes extracted from batteries after 200 charge-discharge cycles, and compared with potential reaction byproducts, as shown in Figures 7 and 8 for BACC and MACC, respectively.

Figure 7 shows the post-mortem X-ray diffraction (XRD) pattern of the BACC electrode after electrochemical cycling, together with reference diffraction patterns of CuO [39], metallic Cu [40], and $CuCl_2$ [41], which were considered as possible secondary phases formed during battery operation.

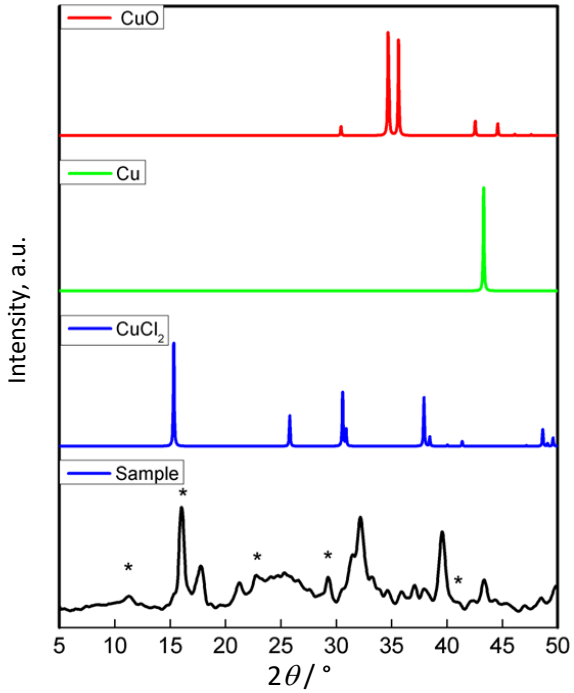

Figure 7. *Post-mortem XRD patterns of the BACC electrode after electrochemical cycling*

The XRD pattern of the cycled BACC electrode exhibits a complex diffraction profile characterized by broadened peaks and a reduced overall crystallinity compared to the pristine material. Nevertheless, several diffraction features marked with * can still be attributed to residual reflections of the original BACC phase, indicating that the material does not undergo complete structural collapse upon cycling but instead retains partial structural integrity. In addition, several diffraction peaks in the experimental pattern coincide with the characteristic reflections of CuO. Furthermore, the appearance of intense reflections matching those of metallic Cu indicates the partial reduction of copper ions during cycling. Additionally, several diffraction peaks in the low and mid-angle regions correspond with the reference pattern of $CuCl_2$, confirming the formation of copper chloride species. The simultaneous detection of residual BACC reflections alongside CuO, Cu, and $CuCl_2$ phases indicates that electrochemical cycling induces partial degradation of the active material. This degradation involves both oxidation and reduction pathways of copper species, as well as chemical reactions with

chloride, leading to the formation of multiple secondary phases. These structural changes are consistent with the increased impedance and altered charge-storage kinetics observed by EIS, supporting the conclusion that structural and chemical degradation contribute to the evolution of the electrochemical performance of the BACC electrode.

Similarly, the post-mortem X-ray diffraction (XRD) patterns of the MACC electrode after electrochemical cycling, presented in Figure 8, are compared with the pristine MACC sample and reference diffraction patterns of CuO, metallic Cu, and $CuCl_2$ to identify possible degradation byproducts. The post-mortem MACC XRD pattern shows a significant reduction in peak intensity together with noticeable peak broadening, suggesting a substantial loss of crystallinity and partial structural degradation of the active material. Despite this degradation, several diffraction features observed in the post-mortem pattern can be correlated with the pristine MACC phase, indicating that the original structure is not completely destroyed during cycling. Nevertheless, the diminished intensity of these reflections indicates that the structural integrity of MACC is more severely affected than in the pristine state.

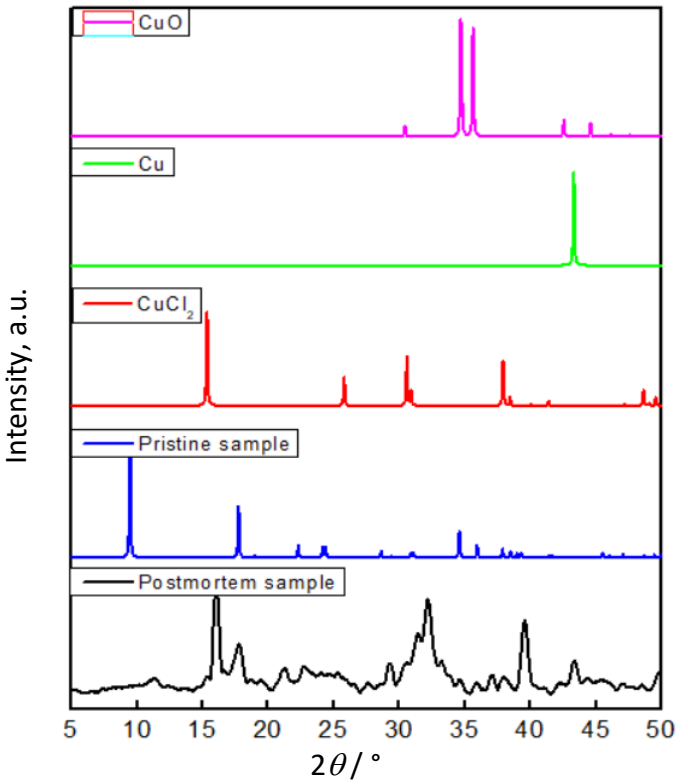

Figure 8. *Post-mortem XRD patterns of the MACC electrode after cycling.*

In addition to the residual MACC-related reflections, several diffraction peaks in the post-mortem pattern closely match those of CuO, confirming the formation of copper oxide species during electrochemical operation. Moreover, intense reflection consistent with metallic Cu is clearly identified, indicating the reduction of copper ions to Cu^0 during cycling. Also, additional diffraction peaks coincide with the reference pattern of $CuCl_2$, confirming the formation of copper chloride species. These structural changes are consistent with the increased impedance observed in EIS, indicating that degradation strongly influences the electrochemical behaviour of MACC.

The post-mortem XRD analysis reveals differences in the structural stability of the BACC and MACC electrodes after electrochemical cycling. In the case of BACC, the XRD pattern still exhibits several residual reflections associated with the pristine material, indicating partial retention of the original crystal structure despite the formation of secondary phases. In contrast, the post-mortem XRD pattern of MACC shows a more pronounced loss of crystallinity, evidenced by broader and less intense

diffraction peaks, suggesting more severe structural degradation. Both materials exhibit the formation of CuO, metallic Cu, and $CuCl_2$ as degradation byproducts, confirming that electrochemical cycling induces irreversible redox transformations and chemical reactions involving copper species.

Overall, the post-mortem XRD results provide the most direct structural evidence of the dominant electrochemical mechanism in BACC and MACC, confirming that charge storage is governed by copper conversion reactions accompanied by irreversible electrode reconstruction. This non-reversible nature limits the long-term electrochemical stability of the studied materials; however, it also positions them as relevant model systems for investigating the relationship among hybrid structure, copper chemistry, and conversion mechanisms in lithium-ion battery electrodes. Xu *et al.* [42] reviewed recent progress in cathode materials for advanced lithium-ion batteries, highlighting the critical roles of cathode chemistry and crystal structure in determining energy density, rate capability, and cycling stability.

Based on the electrochemical signatures and post-mortem structural analysis, the charge storage mechanism in BACC and MACC cannot be described as a purely intercalation-type process. Instead, it involves a combination of surface-controlled (pseudocapacitive) contributions and conversion-type reactions associated with copper redox chemistry.

Interestingly, post-mortem XRD analysis performed at the early stages of cycling shows the disappearance of the original diffraction peaks without the immediate appearance of well-defined new crystalline phases. This suggests that the initial lithiation leads to rapid structural collapse and the formation of poorly crystalline or nanoscale byproducts with low diffracting potential [30]. In contrast, after prolonged cycling (200 cycles), distinct secondary phases, such as Cu, CuO, and $CuCl_2$, become detectable, indicating progressive structural reorganization and crystallization of the reaction products.

Conclusions

In this work, the electrochemical behaviour and structural stability of BACC and MACC hybrid cathode materials were investigated using cyclic voltammetry, electrochemical impedance spectroscopy, and post-mortem X-ray diffraction.

Electrochemical impedance spectroscopy revealed a significant increase in impedance after cycling for both materials, indicating degradation of the electrochemical performance.

Notably, the strong attenuation or disappearance of the principal diffraction peaks during the early stages of cycling suggests that both materials follow a conversion-type reaction mechanism rather than a simple intercalation process.

Post-mortem XRD analysis further confirms these findings, showing partial retention of the original crystal structure in BACC, whereas MACC undergoes a more pronounced loss of crystallinity. In both materials, the formation of secondary phases such as CuO, metallic Cu, and $CuCl_2$, was detected, indicating irreversible redox transformations and chemical decomposition of copper-containing species during electrochemical operation.

The combined electrochemical and structural results demonstrate that BACC exhibits superior structural properties and more stable diffusion-controlled charge storage compared to MACC, which shows extensive degradation. These findings highlight the critical role of structural stability in controlling the long-term electrochemical performance of hybrid copper-based cathode materials and provide valuable insights for the design of more durable hybrid electrodes for lithium-ion batteries.

Acknowledgements: *Alfredo Romero-Contreras acknowledges the financial support provided by the Secretaría de Ciencia, Humanidades, Tecnología e Innovación (SECIHTI), Mexico, through the Post-doctoral Fellowship Program, which made this research possible.*

Conflict of interest: *The authors declare that there is no conflict of interest.*

Funding: *This work was financially supported by the Secretaría de Ciencia, Humanidades, Tecnología e Innovación (SECIHTI), Mexico, through the Postdoctoral Fellowship Program.*

References

[1] K. Hoang, Understanding the electronic and ionic conduction and lithium over-stoichiometry in $LiMn_2O_4$ spinel, *Journal of Materials Chemistry A* **2** (2014) 18271-18280. https://doi.org/10.1039/c4ta04116j

[2] Y. S. Byeon, W. Lee, S. Park, D. Kim, J. Jung, M. Park, W. Yoon, Comprehensive understanding of elemental doping and substitution of Ni-rich cathode materials for lithium-ion batteries *via in situ* operando analyses, *Small Science* **4** (2024) 2400165. https://doi.org/10.1002/smsc.202400165

[3] A. Hebert, N. Z. Galabi, J. M. Sieffert, M. Blangero, E. McCalla, Elucidating the impact of metal doping in $Li_{1.15}(Ni_{0.35}Mn_{0.65})_{0.85}O_2$ cathodes using high-throughput experiments and machine learning, *EES Batteries* **1** (2025) 260-272. https://doi.org/10.1039/d4eb00016a

[4] M. Li, Z. Zhu, Z. Wang, W. Pan, X. Cao, G. Wu, R. Chen, High-quality hybrid perovskite thin films by post-treatment technologies in photovoltaic applications, *Advanced Materials* **36** (2023) 2309428. https://doi.org/10.1002/adma.202309428

[5] M. H. Bagheri, A. A. Khan, S. Shahzadi, M. M. Rana, M. S. Hasan, D. Ban, Advancements and challenges in molecular/hybrid perovskites for piezoelectric nanogenerator application: a comprehensive review, *Nano Energy* **120** (2023) 109101. https://doi.org/10.1016/j.nanoen.2023.109101

[6] M. J. Islam, K. Pal, M. Harun-Ur-Rashid, A. Kumar, M. F. Hossain, N. Asthana, S. Rajendran, S. Vallinayagam, A. Malik, Optical maneuvering of photofunctioning hybrid perovskite for future photonics potential application, *Journal of Molecular Liquids* **408** (2024) 125343. https://doi.org/10.1016/j.molliq.2024.125343

[7] Z. Jia, C. Cheng, X. Chen, L. Liu, R. Ding, J. Ye, J. Wang, L. Fu, Y. Cheng, Y. Wu, Applications of all-inorganic perovskites for energy storage, *Materials Advances* **4** (2022) 79-104. https://doi.org/10.1039/d2ma00779g

[8] N. Vicente, G. Garcia-Belmonte, Methylammonium lead bromide perovskite battery anodes reversibly host high Li-ion concentrations, *The Journal of Physical Chemistry Letters* **8** (2017) 1371-1374. https://doi.org/10.1021/acs.jpclett.7b00189

[9] Z. Huang, C. Yeh, M. Wang, V. W. Lau, H. Tian, C. Shih, Comprehensive study on phase stability of lead-free Sn-based perovskite $FA_xMA_{1-x}SnI_3$, *Materials Today Advances* **24** (2024) 100534. https://doi.org/10.1016/j.mtadv.2024.100534

[10] D. B. Mitzi, K. Chondroudis, C. R. Kagan, Organic-inorganic electronics, *IBM Journal of Research and Development* **45** (2001) 29-45. https://doi.org/10.1147/rd.451.0029

[11] R. Chiara, M. Morana, L. Malavasi, Germanium-based halide perovskites: materials, properties, and applications, *ChemPlusChem* **86** (2021) 879-888. https://doi.org/10.1002/cplu.202100191

[12] C. Han, A. J. Bradford, A. M. Z. Slawin, B. E. Bode, E. Fusco, S. L. Lee, C. C. Tang, P. Lightfoot, Structural features in some layered hybrid copper chloride perovskites: $ACuCl_4$ or A_2CuCl_4, *Inorganic Chemistry* **60** (2021) 11014-11024. https://doi.org/10.1021/acs.inorgchem.1c00705

[13] D. E. Belikova, S. A. Fateev, V. N. Khrustalev, V. Kozhevnikova, A. A. Ordinartsev, A. V. Dzuban, E. A. Goodilin, A. B. Tarasov, Bright luminescence of new low-melting copper (I) chlorides with compact organic cations, *Journal of Materials Chemistry C* **12** (2024) 13537-13544. https://doi.org/10.1039/D4TC02152E

[14] R. Salgado-Pizarro, C. Barreneche, A. Fernández, Synthesis optimization of copper-based layered perovskites as thermal energy storage materials, *Materials Today Chemistry* **30** (2023) 101491. https://doi.org/10.1016/j.mtchem.2023.101491
[15] Y. Kimishima, Magnetic phase transitions in $(C_6H_5CH_2NH_3)_2[CuCl_4]$, *Journal of Magnetism and Magnetic Materials* **90-91** (1990) 301-302. https://doi.org/10.1016/S0304-8853(10)80108-8
[16] S. Becker, U. Behrens, S. Schindler, Synthesis, structure and reactivity of the compound $[Cu(C_7H_7NH_2)Cl]_4$ derived from CuCl and benzylamine ($C_7H_7NH_2$), *Zeitschrift für Anorganische und Allgemeine Chemie* **641** (2014) 430-435. https://doi.org/10.1002/zaac.201400395
[17] S. Löw, J. Becker, C. Würtele, A. Miska, C. Kleeberg, U. Behrens, O. Walter, S. Schindler, Reactions of copper (II) chloride in solution: facile formation of tetranuclear copper clusters and other complexes that are relevant in catalytic redox processes, *Chemistry - A European Journal* **19** (2013) 5342-5351. https://doi.org/10.1002/chem.201203848
[18] W. -Q. Wu, Z. Yang, P. N. Rudd, Y. Shao, X. Dai, H. Wei, J. Zhao, Y. Fang, Q. Wang, Y. Liu, Y. Deng, X. Xiao, Y. Feng, Y. Huang, Bilateral alkylamine for suppressing charge recombination and improving stability in blade-coated perovskite solar cells, *Science Advances* **5(3)** (2019) eaav8925. https://doi.org/10.1126/sciadv.aav8925
[19] Z. Xiao, H. Chen, M. Shi, G. Wu, R. Zhou, Z. Yang, M. Wang, B. Tang, Preparation and characterization of organic-inorganic hybrid perovskite $(C_4H_9NH_3)_2CuCl_4$, *Materials Science and Engineering B* **117** (2005) 313-316. https://doi.org/10.1016/j.mseb.2004.12.052
[20] A. R. Lim, Exploring the potential applications of lead-free organic-inorganic perovskite type $[NH_3(CH_2)_nNH_3]MCl_4$ (n = 2, 3, 4, 5, and 6; M = Mn, Co, Cu, Zn, and Cd) crystals, *Scientific Reports* **14** (2024) 11808. https://doi.org/10.1038/s41598-024-62705-9.
[21] Z. Hu, H. Zhao, Z. Cheng, J. Ding, H. Gao, Y. Han, S. Wang, Z. Xu, Y. Zhou, T. Jia, H. Kimura, M. Osada, Van der Waals force layered multiferroic hybrid perovskite $(CH_3NH_3)_2CuCl_4$ single crystals, *Physical Chemistry Chemical Physics* **22** (2020) 4235-4239. https://doi.org/10.1039/c9cp05976h
[22] P. Zolfaghari, G. A. De Wijs, R. A. De Groot, The electronic structure of organic-inorganic hybrid compounds: $(NH_4)_2CuCl_4$, $(CH_3NH_3)_2CuCl_4$ and $(C_2H_5NH_3)_2CuCl_4$, *Journal of Physics: Condensed Matter* **25** (2013) 295502. https://doi.org/10.1088/0953-8984/25/29/295502
[23] H. Zhao, H. Fu, Z. Hu, Q. Fu, T. Hong, H. Tao, J. Weng, L. Xiong, Z. Cheng, Magnetic hybrid organic-inorganic perovskite $(CH_3NH_3)_2XCl_4$ (X = Mn, Cu, Co) crystals, *CrystEngComm* **23** (2021) 5208-5213. https://doi.org/10.1039/D1CE00679G
[24] K. Zulfa, B. Zahara, A. A. Afkauni, P. Y. D. Maulida, S. Hartati, I. Mulyani, A. Yudhowijoyo, L. J. Diguna, M. H. Mahyuddin, D. Onggo, M. D. Birowosuto, A. Arramel, Elucidating the vibration modes of two-dimensional hybrid copper halide perovskite crystals by FTIR and Raman spectroscopy, *Materials Today: Proceedings* (2024). https://doi.org/10.1016/j.matpr.2024.03.058
[25] V. Augustyn, J. Come, M. A. Lowe, J. W. Kim, P. Taberna, S. H. Tolbert, H. D. Abruña, P. Simon, B. Dunn, High-rate electrochemical energy storage through Li^+ intercalation pseudocapacitance, *Nature Materials* **12** (2013) 518-522. https://doi.org/10.1038/nmat3601
[26] Z. Lu, X. Ren, Pseudocapacitive storage in high-performance flexible batteries and supercapacitors, *Batteries* **11** (2025) 63. https://doi.org/10.3390/batteries11020063
[27] S. Alam, A. Urooj, S. Rehman, M. Z. Iqbal, H. H. Hegazy, Investigation of metal organic frameworks and their derivatives as electrode materials for hybrid energy storage devices, *Materials Chemistry and Physics* **304** (2023) 127877. https://doi.org/10.1016/j.matchemphys.2023.127877
[28] C. Pastor-Fernández, K. Uddin, G. H. Chouchelamane, W. D. Widanage, J. Marco, A comparison between electrochemical impedance spectroscopy and incremental capacity-differential voltage as Li-ion diagnostic techniques to identify and quantify the effects of

degradation modes within battery management systems, *Journal of Power Sources* **360** (2017) 301-318. https://doi.org/10.1016/j.jpowsour.2017.03.042

[29] T. B. Schön, B. T. McAllister, P. Li, D. S. Seferos, The rise of organic electrode materials for energy storage, *Chemical Society Reviews* **45** (2016) 6345-6404. https://doi.org/10.1039/c6cs00173d

[30] P. Poizot, S. Laruelle, S. Grugeon, L. Dupont, J. Tarascon, Nano-sized transition-metal oxides as negative-electrode materials for lithium-ion batteries, *Nature* **407** (2000) 496-499. https://doi.org/10.1038/35035045

[31] R. Verrelli, J. Hassoun, A. Farkas, T. Jacob, B. Scrosati, A new, high performance CuO/$LiNi_{0.5}Mn_{1.5}O_4$ lithium-ion battery, *Journal of Materials Chemistry A* **1** (2013) 15329-15337. https://doi.org/10.1039/c3ta13960c

[32] Y. Dai, S. Zhang, J. Wen, Z. Song, T. Wang, R. Zhang, X. Fan, W. Luo, Metal chloride cathodes for next-generation rechargeable lithium batteries, *iScience* **27** (2024) 109557. https://doi.org/10.1016/j.isci.2024.109557

[33] S. Fleischmann, J. B. Mitchell, R. Wang, C. Zhan, D. Jiang, V. Presser, V. Augustyn, Pseudocapacitance: from fundamental understanding to high power energy storage materials, *Chemical Reviews* **120** (2020) 6738-6782. https://doi.org/10.1021/acs.chemrev.0c00170

[34] H. Avireddy, B. W. Byles, D. Pinto, J. M. D. Galindo, J. J. Biendicho, X. Wang, C. Flox, O. Crosnier, T. Brousse, E. Pomerantseva, J. R. Morante, Y. Gogotsi, Stable high-voltage aqueous pseudocapacitive energy storage device with slow self-discharge, *Nano Energy* **64** (2019) 103961. https://doi.org/10.1016/j.nanoen.2019.103961

[35] Z. Wu, J. Luo, J. Peng, H. Liu, B. Chang, X. Wang, Rational architecture design of yolk/double-shells Si-based anode material with double buffering carbon layers for high performance lithium-ion battery, *Green Energy & Environment* **6** (2021) 517-527. https://doi.org/10.1016/j.gee.2020.06.009

[36] F. Lin, D. Nordlund, T.-C. Weng, Y. Zhu, C. Ban, R.M. Richards, H.L. Xin, Phase evolution for conversion reaction electrodes in lithium-ion batteries, *Nature Communications* **5** (2014) 3358. https://doi.org/10.1038/ncomms4358

[37] F. Wang, R. Robert, N.A. Chernova, N. Pereira, F. Omenya, F. Badway, X. Hua, M. Ruotolo, R. Zhang, L. Wu, V. Volkov, D. Su, B. Key, M.S. Whittingham, C.P. Grey, G.G. Amatucci, Y. Zhu, J. Graetz, Conversion reaction mechanisms in lithium ion batteries: Study of the binary metal fluoride electrodes, *Journal of the American Chemical Society* **133** (2011) 18828-18836. https://doi.org/10.1021/ja206268a

[38] N. Vicente, D. Bresser, S. Passerini, G. Garcia-Belmonte, Probing the 3-step Lithium Storage Mechanism in $CH_3NH_3PbBr_3$ Perovskite Electrode by Operando-XRD Analysis, *ChemElectroChem* **6(2)** (2018) 456-460. https://doi.org/10.1002/celc.201801291

[39] Crystallography Open Database, Copper(II) oxide (CuO, tenorite) crystal structure (COD entry 1011194), https://www.crystallography.net/1011194.cif (accessed 24 February 2026).

[40] K. Persson, Materials data on Cu by Materials Project, OSTI OAI (U.S. Department of Energy Office of Scientific and Technical Information) (2020). https://doi.org/10.17188/1204433

[41] K. Persson, Materials data on $CuCl_2$ by Materials Project, OSTI OAI (U.S. Department of Energy Office of Scientific and Technical Information) (2020). https://doi.org/10.17188/1205331

[42] B. Xu, D. Qian, Z. Wang, Y. S. Meng, Recent progress in cathode materials research for advanced lithium-ion batteries, *Materials Science and Engineering: R: Reports* **73** (2012) 51-65. https://doi.org/10.1016/j.mser.2012.05.003